Document Version
Final published version

Citation (APA)
Karanth, P., Weijers, M., Lavrinenko, A. K., Izelaar, B., Kortlever, R., Ganapathy, S., Wagemaker, M., & Mulder, F. M. (2025). Designing Fluorine-Free Electrolytes for Lithium Metal Batteries. *Journal of the American Chemical Society*, *147*(50), 46008-46022. https://doi.org/10.1021/jacs.5c12584

JACS
JOURNAL OF THE AMERICAN CHEMICAL SOCIETY

pubs.acs.org/JACS

Article

Designing Fluorine-Free Electrolytes for Lithium Metal Batteries

Pranav Karanth, Mark Weijers, Anastasia K. Lavrinenko, Boaz Izelaar, Ruud Kortlever, Swapna Ganapathy, Marnix Wagemaker, and Fokko M. Mulder*

Cite This: *J. Am. Chem. Soc.* 2025, 147, 46008−46022

Read Online

ACCESS | Metrics & More | Article Recommendations | Supporting Information

ABSTRACT: Fluorination of electrolytes has been a widely used strategy to enable stable cycling in lithium metal batteries. However, a move toward fluorine-free electrolytes is desirable given the safety and environmental concerns surrounding fluorinated materials. Designing these electrolytes requires a comprehensive understanding of bulk electrolyte and interfacial properties in the absence of fluorine, particularly the solvation structures surrounding Li^+ and the solid electrolyte interface (SEI) composition. Among fluorine-free Li salts, lithium nitrate ($LiNO_3$) is often used to obtain highly ion-conductive SEI components. However, its poor ion dissociation and rapid consumption upon freshly plated lithium currently hinder its use as the main electrolyte salt. Herein, we show that the modification of Li^+ inner solvation structures by employing lithium bis(oxalato)borate (LiBOB) as the secondary salt in $LiNO_3$/diglyme electrolytes synergistically improves both bulk Li^+ transport and SEI properties. It significantly enhances ion dissociation, which increases the ionic conductivity of the electrolyte despite an increase in its viscosity. Furthermore, the presence of LiBOB-derived outer SEI components over the $LiNO_3$-derived ion-conductive inner SEI layer results in low-surface-area Li deposits and lower Li^+/anion consumption during cycling. The dual-salt fluorine-free electrolyte enables stable, long-term cycling in Li/Cu cells for >700 cycles and shows promising capacity retention in Li/LFP full cells at ambient temperature. Our work highlights the importance of tuning the Li^+ solvation structures for optimizing bulk and interface properties in fluorine-free electrolytes and presents a viable pathway toward the development of greener electrolytes for lithium metal batteries.

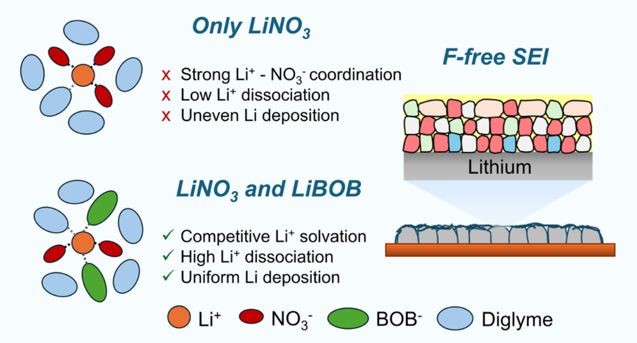

INTRODUCTION

Lithium metal batteries (LMBs) have been subjected to significant research and commercial interest over the past two decades, owing to the promise of improved cell-level energy densities when employing lithium metal as the anode.[1] A major challenge in realizing LMBs has been stabilizing lithium plating and stripping, particularly due to the (electro) chemical instability of Li metal in traditional carbonate electrolytes and dendritic metal growth at moderate to high current densities.[2,3] However, a reasonable amount of success has been achieved by modifying the fluorine content in electrolytes, either by changing the salt,[4] having fluorinated cosolvents/additives,[5−7] fluorinating traditional solvents,[8,9] and having fluorinated diluents.[10−13] The improved Li metal stability in these reports is often attributed to the LiF-rich SEI,[4] while the use of fluorinated solvents/cosolvents was also shown to additionally improve the chemical stability of the SEI[7] and the electrochemical stability windows for electrolytes that would otherwise be unstable at high voltages.[8,9]

However, the fluorination of battery electrolytes gives rise to several environmental and safety hazards. Several fluorinated components in batteries, including electrolyte salts, such as LiTFSI, and hydrofluoroether diluents used in localized high-concentration electrolytes, are perfluoroalkyl substances (PFAS), which are compounds with multiple F atoms attached to an alkyl chain. Thanks to the robust C−F bond, these compounds are extremely durable[14] but also very difficult to recycle. Exposure to PFAS materials has been linked to a range of health disorders in animals and humans, including cancer,[15,16] and therefore, several global organizations, including the European Union, have proposed a ban on the use of PFAS materials.[17] Besides PFAS, several other fluorinated materials such as $LiPF_6$ and FEC are known to produce toxic hydrogen fluoride (HF) during cycling and in substantially higher amounts during accidents such as battery fires.[18] Another factor to be considered here is the cost, as fluorinated salts, solvents, and diluents are more expensive compared to their nonfluorinated counterparts (Figure S1), putting their commercial feasibility into question. Therefore,

Received: July 23, 2025
Revised: November 20, 2025
Accepted: November 24, 2025
Published: December 4, 2025

https://doi.org/10.1021/jacs.5c12584

while fluorinated electrolytes possess several benefits, moving toward cleaner and safer fluorine-free electrolytes is highly desirable. Furthermore, growing evidence suggests that fluorine may not be indispensable to high Li plating/stripping efficiencies. Recent reports have shown that LiF does not form a continuous passivation layer in the SEI of fluorinated electrolytes and could be acting as an indirect SEI/inert block that can stabilize Li electrodeposition by increasing Li^+ surface diffusivity or homogenizing the Li^+ diffusion field gradient.[19,20] Lithium oxide (Li_2O), typically also found as an SEI component in most high-performance LMB electrolytes, is more ionically conductive than LiF[21] and has been shown to form a continuous layer in high-Coulombic-efficiency (CE) electrolytes. A recent study by Hobold et al. also suggested that the CEs in LMBs correlate much better with the Li_2O content in the SEI than the LiF content, and the nature of Li_2O layers in the SEI dictates the CE. A high Li_2O content in the SEI, therefore, could be a crucial factor in the design of highly efficient F-free electrolytes.[22]

$LiNO_3$ is an inexpensive salt additive often used in high-CE electrolytes for LMBs and is known to preferentially reduce to form a highly conducting interphase consisting of Li_2O and Li_3N.[22,23] However, its use as the main electrolyte salt has been hindered by several challenges. $LiNO_3$ possesses a high donor number (~22) and is, as a result, poorly soluble in most traditional solvents, including carbonates.[24,25] Studies employing $LiNO_3$ as the main salt, therefore, use high-donor-number solvents such as diethylene glycol dimethyl ether (diglyme, G2),[26,27] triethyl phosphate (TEP),[28,29] and dimethyl sulfoxide (DMSO).[24] Moreover, solvated $LiNO_3$ can still retain strong $Li^+{-}NO_3^-$ interactions, leading to significant ion pairing and aggregation. If not sufficiently overcome, then this negatively influences Li^+ dissociation and the ionic conductivity of the electrolyte. $LiNO_3$ can also react with freshly deposited Li metal every cycle, resulting in its rapid consumption.[27] Strategies used to enable $LiNO_3$ as the main salt in LMB electrolytes typically involve the use of fluorinated materials. These include the use of "film-forming" additives such as fluoroethylene carbonate (FEC),[7,28,29] inclusion of a secondary salt,[27] and employing polymerization inhibitors such as hexafluoroisopropanol.[26] More recently, "fluorine-free" strategies employing $LiNO_3$ and an additional salt have also been reported for Li metal batteries.[30,31]

In the context of fluorine-free electrolyte design, particularly for $LiNO_3$-based systems, it is essential to arrive at a comprehensive understanding of their bulk transport properties and interfacial stability with Li metal. Both these aspects are influenced by the Li^+ solvation environment, particularly the inner solvation sheath, and elucidating its structure is crucial to understanding the changes to the electrolyte upon cosalt/solvent addition.[32] Furthermore, the surface area of the Li deposits formed can also strongly influence the durability of these electrolytes. While the Li_2O/Li_3N-containing SEI derived from $LiNO_3$ is expected to display high Li^+ conductivity, the mechanical fragility of this SEI could lead to fresh Li deposition in every cycle, increasing the overall Li surface area. The strongly oxidizing nature of the NO_3^- ion leads to its reactivity with this fresh Li and its consumption.[28,33] Here, modulating the depthwise composition of the SEI using suitable additives could be a strategy to influence both the mechanical stability of the SEI and the surface area of Li deposition.

In this work, we design $LiNO_3$-based fluorine-free electrolytes for LMBs and elucidate the effects of lithium bis(oxalato)borate (LiBOB) as a secondary salt in synergistically altering both the bulk ion transport in the electrolyte and the interfacial stability with Li metal. The changes to the ion transport properties and the solvation structures in these electrolytes are studied using spectroscopic techniques and molecular dynamics (MD) simulations. The resulting differences in the lithium microstructure and its SEI composition are elucidated through operando NMR and ex situ characterization. We show that the relative increase in LiBOB content significantly alters the Li^+ inner solvation structures, which in turn increases the degree of ion dissociation, leading to higher ionic conductivities. Furthermore, this also changes the SEI composition, resulting in uniform, low-surface-area Li deposits and leading to lower Li^+/anion consumption into the SEI (with cycling) and prolonged cycle life. We demonstrate that such a dual-salt fluorine-free electrolyte achieves stable cycling in Li/Cu cells for over 700 cycles and shows promising capacity retention in $Li/LiFePO_4$ (LFP) full cells with commercial active mass loadings (86.7% after 100 cycles) at ambient temperature. Our work provides key insights into the composition-dependent ion dynamics and Li interface properties in $LiNO_3$-based ether electrolytes and presents a viable pathway for the development of safe, room-temperature fluorine-free electrolytes.

■ RESULTS AND DISCUSSION

Choice of Salts, Solvents, and Salt Concentration. The choice of constituents for $LiNO_3$-based fluorine-free electrolytes in this study is based on the expected ion transport properties, electrochemical stability, and safety. Among the high-donor-number solvents suitable for $LiNO_3$-based electrolytes, diglyme (G2) presents a good balance of solvent properties: a high donor number (~24),[34] a higher flash point compared to common battery electrolyte solvents (57.3 °C), and a moderate viscosity (~1 cP at 20 °C).[35] While increasing the salt concentration to generate anion-derived SEI on lithium is a well-known strategy to boost CEs in ether electrolytes, excessively high salt concentrations could detrimentally affect the ion transport properties of the electrolyte, lowering the room-temperature conductivity. We chose an overall salt:solvent molar ratio of 2.4:7 (with 7 mol of diglyme corresponding to about 1 L of diglyme at 25 °C) based on the ion transport properties previously reported for $LiNO_3$/diglyme-based electrolytes at similar concentrations.[26]

As previously discussed, a stable SEI that can regulate Li^+/anion reactivity with the Li metal is crucial for the long-term stability of these electrolytes. In this regard, the incorporation of LiBOB as the secondary salt is particularly interesting. LiBOB, a noncorrosive, halogen-free salt, has previously been looked at as an alternative to $LiPF_6$ in Li-ion batteries[36] and shows similar properties such as passivation of both the graphite anode and Al current collector.[37,38] While its room-temperature ionic conductivity as a standalone electrolyte salt is limited, it displays enhanced temperature stability.[30,36] Additionally, the choice of solvent (diglyme) and salts ($LiNO_3$ and LiBOB) results in reduced flammability (i.e., no flammability observed for 5 s) for these electrolytes in comparison to standard carbonate-based electrolytes such as 1 M $LiPF_6$ in EC:DMC (1:1 vol %) hereafter referred to as LP30 (Figure S2) and electrolytes based on low-flash-point ethers like dimethoxyethane (DME). To elucidate the effect of

$LiNO_3$/LiBOB salt ratios on bulk electrolyte properties and interfacial stability with Li metal, we investigated three distinct salt ratios, and the details of their composition are provided in Table 1.

Table 1. Electrolytes Studied and Their Compositions[a]

electrolyte name	$LiNO_3$ (mol)	LiBOB (mol)	diglyme (mol)	density at 25 °C (g cm^{-3})	total molarity (M)
2.4LN-0LB	2.4	0	7	1.03	2.24
2LN-0.4LB	2	0.4	7	1.08	2.24
1.2LN-1.2LB	1.2	1.2	7	1.11	2.12

[a] Molarities were calculated based on density measurements at 25 °C. LN stands for $LiNO_3$ and LB for LiBOB.

Changes to Bulk Transport Properties and Solvation Structure. The addition of LiBOB to the fluorine-free electrolyte is expected to proportionately increase its viscosity owing to the higher presence of the bulkier BOB^- anion. Indeed, we observe that the dynamic viscosity of the electrolytes rises from 9.1 cP for the 2.4LN-0LB electrolyte to 14.4 cP for the 1.2LN-1.2LB electrolyte at 20 °C (Figure 1a, additional temperatures shown in Figure S3a). The pulsed field gradient (PFG) NMR results (Figure S3b, errors from fit uncertainty tabulated in Tables S1 and S2) also show a decreasing trend for both Li (^7Li) and solvent (^{13}C corresponding to the solvent peak "b" at ∼71 ppm, shown in Figure S4) self-diffusivities with an increasing LiBOB concentration. However, while the solvent self-diffusivities are higher for all of the studied salt concentrations, the relative Li diffusivity, D_{Li}/D_{Sol} increases from 0.37 for the 2.4LN-0LB electrolyte to 0.48 for the 1.2LN-1.2LB electrolyte (at 25 °C), which suggests changes in Li^+ ion transport properties with an increasing BOB^- content.

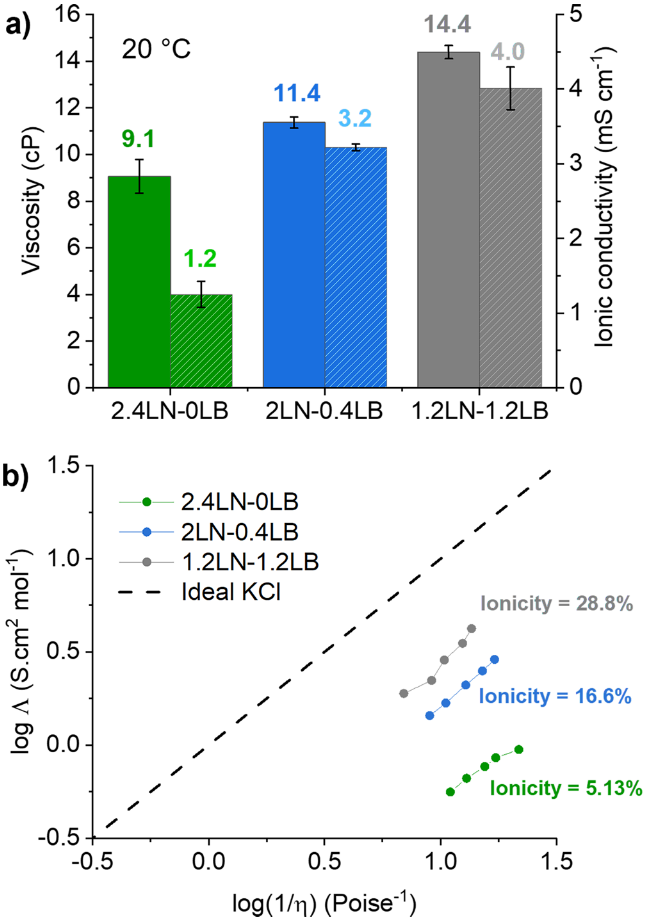

Figure 1. Physical characterization of F-free electrolytes: (a) Viscosity and (electrochemical) ionic conductivity of the electrolytes at 20 °C. Error bars for viscosity indicate 95% confidence intervals for the values obtained through least-squares linear extrapolation to zero stress. Error bars for conductivity represent the standard deviation of replicate cells. (b) Walden plot for the electrolytes along with the "ideal KCl" line.

In contrast to the viscosity/self-diffusivity trends, the electrochemically measured total ionic conductivity of the electrolytes, sensitive to the charge carrier concentration in the system, shows a significant increase with the increasing LiBOB content, i.e., from 1.2 mS cm^{-1} for the 2.4LN-0LB electrolyte to 4.0 mS cm^{-1} for the 1.2LN-1.2LB electrolyte at 20 °C (Figure 1a), which further increases to 8.9 mS cm^{-1} at 60 °C. Figure 1b shows a Walden plot (a log−log plot of molar ionic conductivities against dynamic viscosities at different temperatures) for the F-free electrolytes for a temperature range of 20−60 °C. Here, the resulting plot lines are compared with the "ideal KCl" line resulting from a 1 M aqueous solution, to roughly estimate the "ionicity" of the electrolytes.[39−42] Ionicity is a measure of the extent to which ionic self-diffusion contributes to ionic conductivity and provides an estimate of ion dissociation, with the "ideal KCl" line representing a fully ion-dissociated system.[40] A low ionicity of 5.13% is obtained for the 2.4LN-0LB electrolyte, and this value significantly increases with the amount of LiBOB in the system, i.e., to 16.6% for the 2LN-0.4LB electrolyte and to 28.8% for the 1.2LN-1.2LB electrolyte (calculation methodologies discussed further in Supporting Information Note 1).

For anions with a high Lewis basicity/donor number such as NO_3^-, Li^+−anion bonds typically possess high dissociation energies, resulting in low ion dissociation in concentrated glyme solutions.[40] We observe that the addition of LiBOB into these systems results in higher ion dissociation, which is likely a combined effect of easier LiBOB salt dissociation and weakened Li^+−NO_3^- interactions. We investigate this mechanism further by experimentally and computationally studying the changes in the Li^+ solvation structure. The chemical structures and the corresponding electrostatic potential surfaces for the species present in the investigated system are shown in Figure 2a, which indicates the stronger electron-withdrawing nature of the coordinating oxygens in NO_3^- compared to those in BOB^- and diglyme. With ^7Li NMR (Figure 2b), an upfield shift (i.e., a shift to lower ppm values) is observed with an increasing LiBOB content (from −0.025 ppm for the 2.4LN-0LB electrolyte to −0.58 ppm for the 1.2LN-1.2LB electrolyte). The upfield shift indicates a higher shielding due to increased Li^+ coordination from less electron-withdrawing groups, in this case BOB^- ions and/or diglyme molecules. The ^{17}O NMR measurements conducted at 40 °C (Figure 2c, spectra over a wider chemical shift range shown in Figure S6) show an increased broadening of the peaks corresponding to diglyme oxygens (denoted as "a" and "b") a small upfield shift of the peaks (−21.7 to −23.8 ppm for environment "a") indicating a higher electron density around the diglyme oxygens with an increasing LiBOB content, both of which suggest an increase in the coordination of diglyme with Li^+, leading to lower solvent mobility. The increased

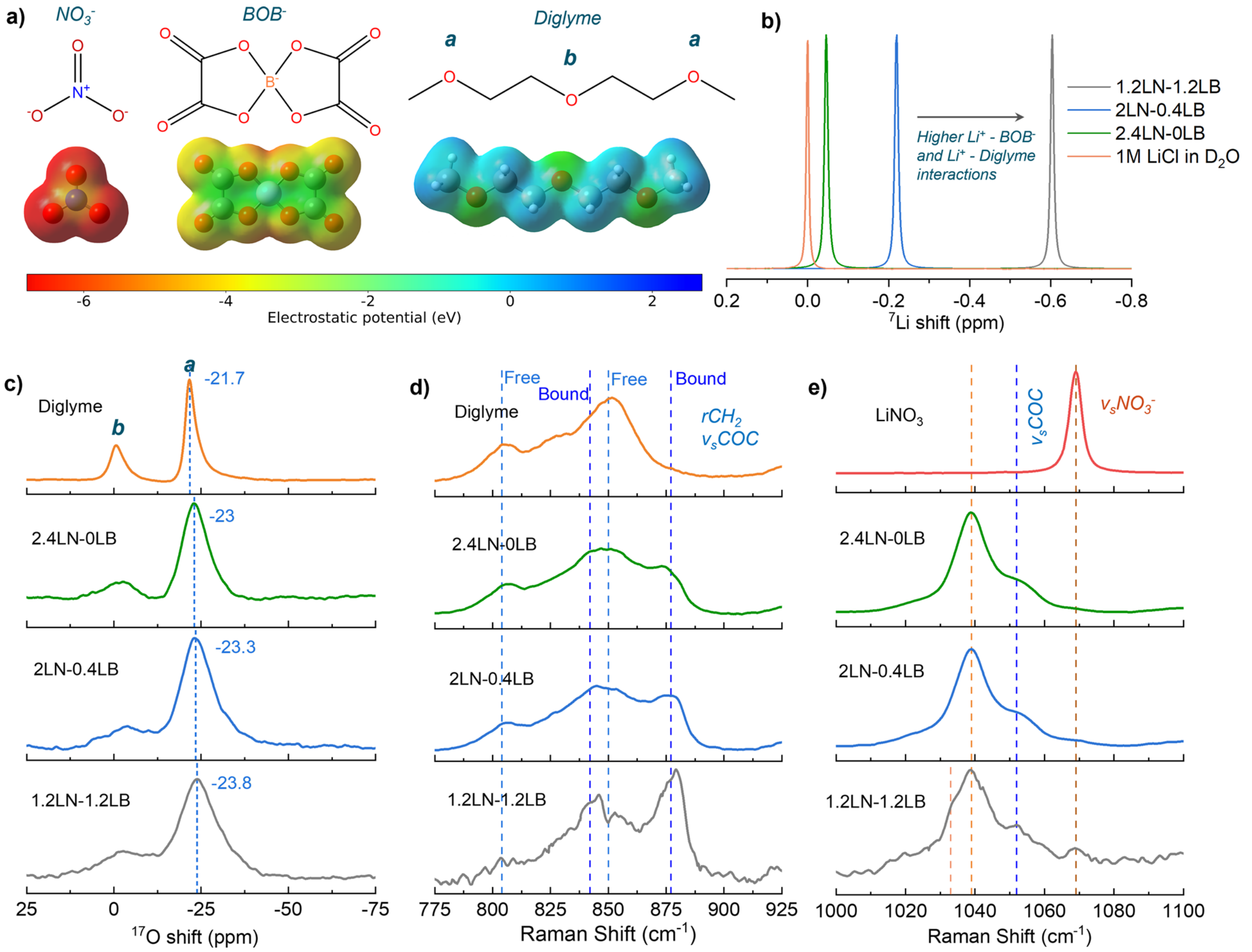

Figure 2. Investigation of solvation structures in fluorine-free glyme electrolytes: (a) Chemical structures and electrostatic potential (ESP) surface maps of NO_3^-, BOB^-, and diglyme. (b) ^{7}Li NMR at 25 °C. (c) Zoomed inset of ^{17}O solution NMR at 40 °C. (d) Raman spectra for electrolytes and diglyme in the region corresponding to CH_2 rocking and C−O−C stretching vibrations. (e) Raman spectra for electrolytes and $LiNO_3$ in the region corresponding to NO_3^- stretching vibrations.

shielding of diglyme oxygens with LiBOB incorporation is also evident from the ^{13}C NMR results (Figure S4), where the ^{13}C environments adjacent to the oxygens also show a similar upfield shift. These trends are also reflected in the Raman spectroscopy results for the 775−925 cm^{-1} region corresponding to CH_2 rocking and C−O−C stretching vibrations in glymes (Figure 2d, spectra over a wider range shown in Figure S7).[43,44] For all the F-free electrolytes, in addition to the "free" glyme environment at around 803 and 850 cm^{-1}, additional "bound" glyme peaks corresponding to coordination with alkali metal cations emerge at 840 and 877 cm^{-1},[43] with the amount of "bound" diglyme increasing from 2.4LN-0LB to 1.2LN-1.2LB electrolytes. Furthermore, in comparison to solid $LiNO_3$, the peak corresponding to NO_3^- stretching vibrations at 1069 cm^{-1} shifts to a lower wavenumber of around 1039 cm^{-1} upon dissolution (Figure 1e). For the 1.2LN-1.2LB electrolyte, however, an additional shoulder feature emerges at a lower wavenumber of 1033 cm^{-1}, which could indicate an increased heterogeneity of the NO_3^--containing solvation structures. Both the NMR and Raman results indicate more competitive Li^+ solvation upon LiBOB incorporation, which could explain the higher ionicity compared to that of the 2.4LN-0LB electrolyte (Figure 1b).

Molecular dynamics (MD) simulations were performed to obtain a deeper understanding of the solvation structure changes upon the LiBOB introduction. The radial distribution functions (RDF) together with oxygen coordination number analysis (Figure 3a,b) show that at low LiBOB contents, Li^+ is predominantly coordinated by the NO_3^- species. As the LiBOB concentration increases, the average first-shell coordination number of NO_3^- drops from 3.21 to 1.48, while the contributions from BOB^- and diglyme grow. Notably, the total anion coordination of Li^+ (both NO_3^- and BOB^-) remains approximately the same, suggesting that the inner solvation sheath of Li^+ is anion-dominated across all three electrolytes. The unchanged position of the first Li^+-NO_3^- RDF peak, upon adding LiBOB, can be attributed to the smaller size of the NO_3^- anion, which allows it to pack more closely around the Li^+ ion compared to the larger BOB^- anion. Although NO_3^- can approach Li^+ at the same distance, it appears less frequently in the first shell when BOB^- is present, indicating weaker Li^+−NO_3^- coordination.

Looking at the possible solvation structures (Figure 3c−e, simulation boxes shown in Figure S8, and detailed lists of all simulation structures provided in Figure S9), it is clear that the solvation structures are predominantly anion-rich in all three cases. However, increasing the relative amount of LiBOB in the electrolyte results in higher participation of BOB^- in the inner solvation structure, as indicated by the dominant solvation

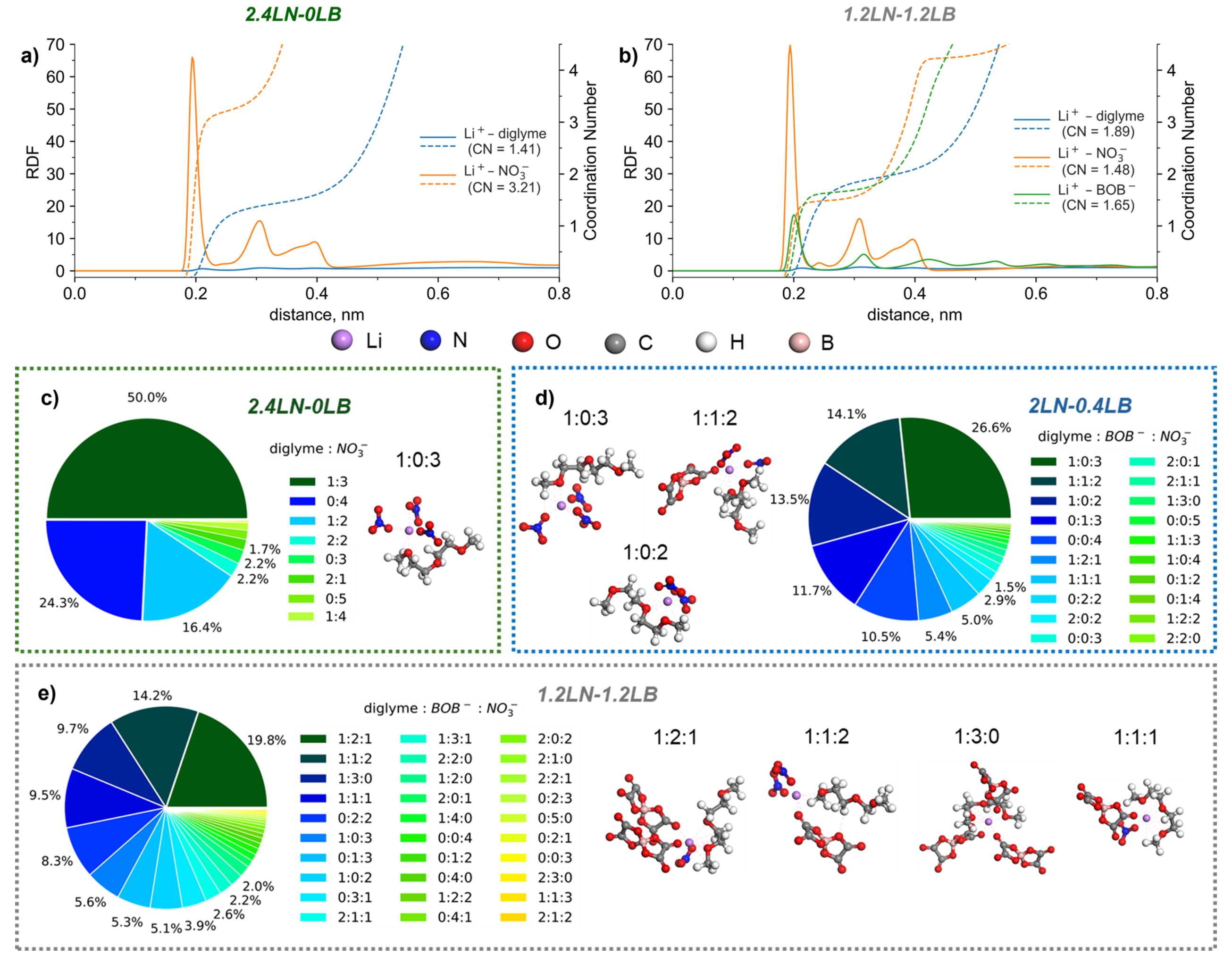

Figure 3. Molecular dynamics (MD) analysis of fluorine-free electrolytes. Top: radial distribution function (RDF) (solid line) and coordination number (CN) (dashed line) between Li^+ and surrounding molecules and ions in (a) 2.4LN-0LB and (b) 1.2LN-1.2LB electrolytes. The CN of Li^+-diglyme, Li^+-NO_3^-, and Li^+-BOB^- were extracted at the first prominent minimum of RDF around 0.32, 0.25, and 0.27 nm, respectively. Bottom: pie charts of Li^+ coordination environments and dominant solvation structures (making up ∼50% of all the solvation structures) obtained from MD simulations for (c) 2LN-0.4LB, (d) 2LN-0.4LB, and (e) 1.2LN-1.2LB electrolytes. For the 2.4LN-0LB electrolyte, the ratios indicate $N_{Diglyme}$:$N_{NO_3^-}$, while for the other two, the ratios indicate $N_{Diglyme}$: N_{BOB^-}: $N_{NO_3^-}$.

structures, and higher diversity of solvation structures, as indicated by the pie charts.

While these results suggest that the inner solvation structures remain anion-dominated for the investigated NO_3^-/ BOB^- ratios, the addition of steric BOB^- ions into the inner solvation sheath, coupled with the progressive increase in the heterogeneity of solvation structures (which increases the configurational entropy of the system), is suggested to be contributing to the overall decrease in Li^+ coordination by NO_3^- and more competitive solvation by $BOB^-$and diglyme. This explains the increase in Li^+−diglyme coordination strength as indicated by Raman and ^{17}O NMR results and also the drop in solvent diffusivity, as seen with PFG-NMR and further confirmed by the mean square displacement (MSD) results (Figure S8). More importantly, the decrease in Li^+−NO_3^- ion pairing also leads to observed higher ion dissociation and higher ionic conductivity. Therefore, the inclusion of LiBOB in the system, despite causing a reduction in the bulk self-diffusion properties, results in synergistic improvements to Li^+ transport in the electrolyte, rendering it suitable for application in room-temperature lithium metal batteries.

Lithium Plating/Stripping in Li/Li and Li/Cu Cells. The changes to Li^+ solvation in $LiNO_3$/diglyme electrolytes with LiBOB addition are expected to impact both the rate capability and stability against Li metal. To understand these better, we evaluated the electrochemical performance of these fluorine-free electrolytes in Li−Li and Li/Cu cells. The kinetics of Li plating/stripping in liquid electrolytes is dictated by the exchange current density at the Li/electrolyte interface, which practically depends on both Li^+ desolvation (related to bulk conductivity) and Li^+ conductivity through the SEI.[45] Figure 4a shows the Tafel plots extracted from the fifth cyclic voltammetry (CV) scan conducted in Li/Li cells (at a rate of 0.5 mV s^{-1}, CV scans shown in Figure S10). Here, the highest pseudoexchange current density, j_{ex}^{P} (which includes SEI and surface area change contributions),[45] is observed for the 2LN-0.4LB electrolyte (0.80 mA cm^{-2}), followed by 1.2LN-1.2LB (0.28 mA cm^{-2}) and 2.4LN-0LB (0.12 mA cm^{-2}) electrolytes.

However, for long-term stability, we observe a different trend for the Li/Li cells cycled at 1 mA cm^{-2} and 1 mAh cm^{-2}

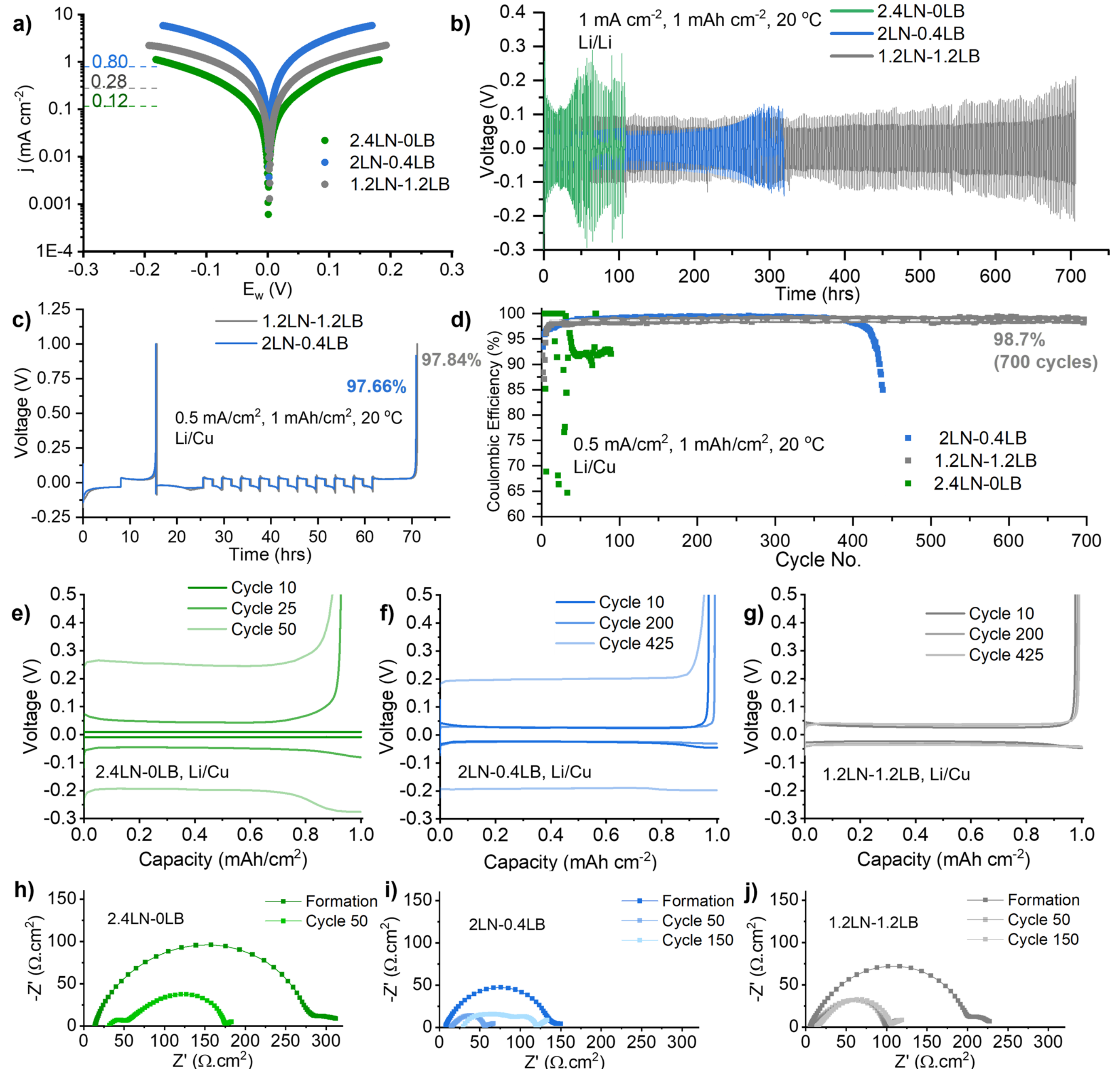

Figure 4. Electrochemical performance in Li/Li and Li/Cu cells: (a) Tafel plots extracted from the 5th cyclic voltammetry scan performed in Li/Li cells (at 0.5 mV s^{-1}). Pseudo-exchange current density, j_{ex}^{P} in mA cm^{-2} for the electrolytes, is indicated on the left. (b) Voltage profiles of Li/Li cells at 1 mA cm^{-2} (capacity, 1 mAh cm^{-2}). (c) Voltage measurements in Li/Cu cells at 0.5 mAh cm^{-2} and 1 mAh cm^{-2} with a reservoir plating of 5 mAh cm^{-2}. (d) Coulombic efficiency measurements in Li/Cu cells at 0.5 mAh cm^{-2} and 1 mAh cm^{-2} without reservoir plating. (e) Voltage profiles of Li/Cu cells (0.5 mA cm^{-2}; capacity, 1 mAh cm^{-2}) at the 10th, 25th, and 50th cycles for the 2.4LN-0LB electrolyte. Voltage profiles of Li/Cu cells at the 10th, 200th, and 425th cycles are provided for (f) 2LN-0.4LB and (g) 1.2LN-1.2LB cells. EIS Nyquist plots of Li/Li cells after formation, cycle 50, and cycle 150 are provided for (h) 2.4 LN- 0LB, (i) 2LN-0.4LB, and (j) 1.2LN-1.2LB cells.

at 20 °C (Figure 4b, with the zoomed insets of voltage traces at different times displayed in Figure S11). The 2.4LN-0LB electrolyte exhibits a high overpotential (>0.1 V), and the voltage trace turns unstable at ∼55 h, suggesting irregular Li plating/stripping leading to dendrites/soft shorts. The 2LN-0.4LB electrolyte has the lowest overpotential initially, consistent with its high j_{ex}^{P} value, but this increases after ∼250 h, becoming similar to the initial overpotential in the 2.4LN-0LB electrolyte and leading to cell failure (by soft-shorting) after ∼300 h. For the 1.2LN-1.2LB electrolyte, the overpotential slightly increases, particularly toward the end of the plating/stripping cycle, where the “peaking” behavior becomes more pronounced. This behavior has been attributed to the concentration polarization-induced overpotential for lithium plating and stripping,[46] but it could also indicate the formation of a more electronically passivating SEI that prevents soft shorts.[47] Consequently, the cycle life of the F-free electrolytes significantly improves with an increasing LiBOB content, with the 1.2LN-1.2LB electrolyte showing stable cycling for over 700 h. Furthermore, the voltage trace from an intermediate “1.6LN-0.8LB” composition (Figure S12) further

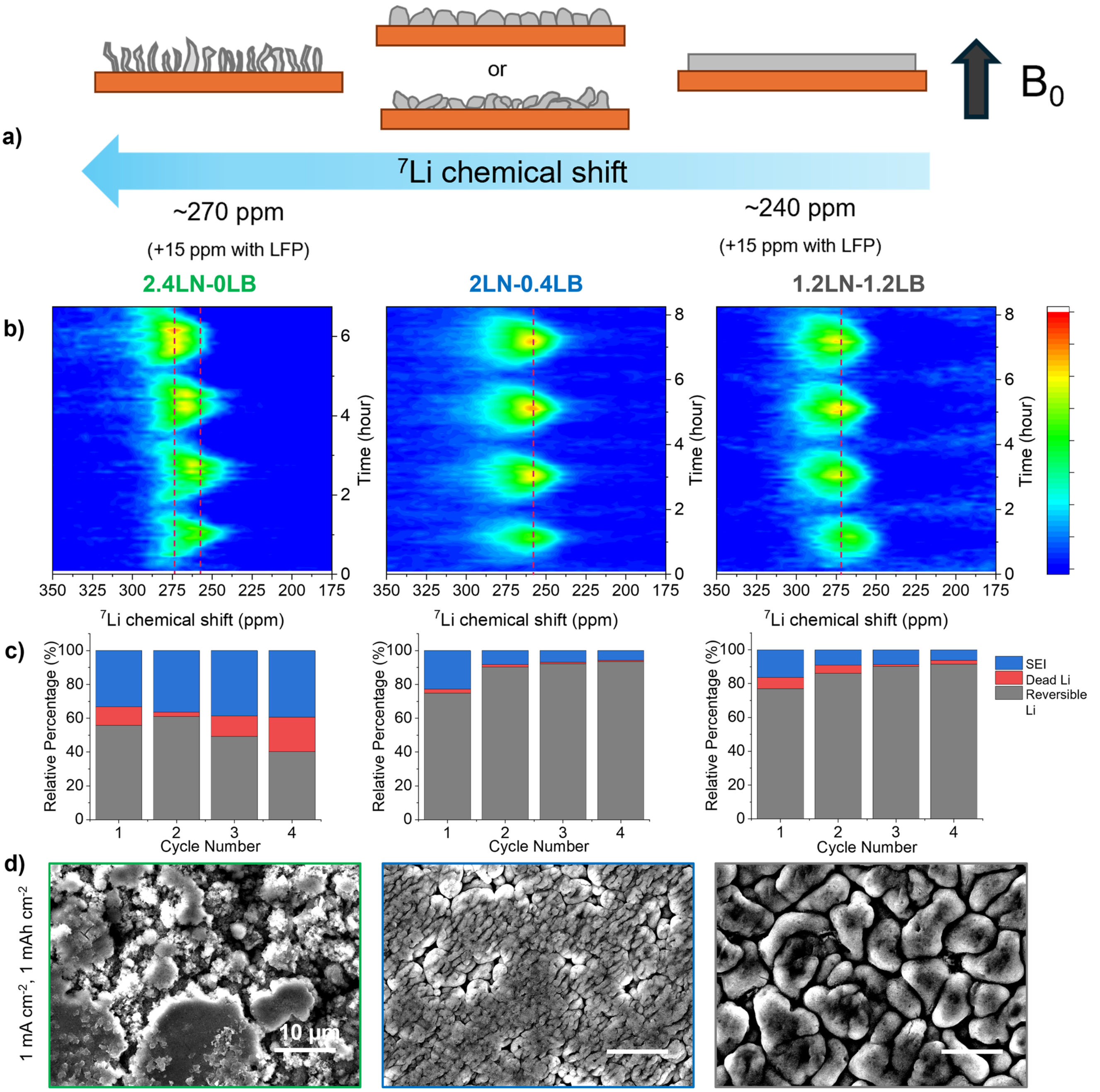

Figure 5. Initial Li deposition morphology in fluorine-free electrolytes: (a) Schematic diagram showing the variations in the ^{7}Li chemical shift depending on the orientation of Li metal with respect to magnetic field B_0. (b) Evolution of the metallic ^{7}Li chemical shift in Cu/LiFePO$_4$ cells cycled for 4 cycles at 0.5 mA cm^{-2} and 0.5 mAh cm^{-2} (1 h) plating per cycle. (c) Percentage of Li utilization per cycle to reversible Li, SEI, and dead Li. (d) Top-view SEM images of 1 mAh cm^{-2} electrodeposited Li on Cu; the scale bar is 10 μm. For (b), (c), and (d), left to right, the images correspond to 2.4LN-0LB, 2LN-0.4LB, and 1.2LN-1.2LB electrolytes, respectively.

demonstrates that the long-term stability in these electrolytes correlates directly with the LiBOB content.

We also evaluated the Coulombic efficiencies (CE) of fluorine-free electrolytes in Li/Cu cells with 0.5 mAh cm^{-2} and 1 mAh cm^{-2} Li plating per cycle, according to both the reservoir-based and conventional methods,[48] with a reservoir plating of 5 mAh cm^{-2} for the former (Figure 4c). While the 2.4LN-0LB electrolyte could not be evaluated due to cell failure during the reservoir plating, the 2LN-0.4LB and 1.2LN-1.2LB electrolytes show high average CEs of 97.66% and 97.84%, respectively (Figure S13) compared to 87.50% for the standard LP30 electrolyte (Figure S14). On long-term cycling with the conventional method, the 2LN-0.4LB electrolyte shows a high average CE of 99.08% (Figure S13), but the cell fails after 440 cycles (Figure 4d). In contrast, the 1.2LN-1.2LB cell cycles for over 700 cycles in line with the trends observed for Li/Li cells. An average CE of 98.40% is obtained over 400 cycles (Figure S13), which increases to 98.7% over 700 cycles. From the Li plating/stripping voltage traces of Li/Cu cells (Figure 4e−g), it is clear that with cycling, the ohmic drop increases within a few cycles (10−50) for the 2.4LN-0LB electrolyte, and this could be caused by a low concentration of free charge carriers, particularly Li^{+}, which is expected for this composition due to strong Li^{+}−NO$_3^{-}$ interactions leading to poor Li^+ dissociation (Figure 1b). Here, the presence of the BOB^- ion improves the charge carrier concentration, leading to a lower ohmic drop for the 2LN-0.4LB and 1.2LN-1.2LB electrolytes. With prolonged cycling, particularly beyond 425 cycles (Figure 4f and Figure S15), a similar increase in the ohmic drop is also observed for the 2LN-0.4LB electrolyte. While both NO_3^- and BOB^- ions participate in the inner solvation structure of Li^+ and are expected to decompose to form the SEI, we believe that the drop in the BOB^- concentration to near-zero levels leads to the observed changes to the voltage trace. To further verify this, we performed ^7Li and ^{13}C NMR on the 2LN-0.4LB electrolyte retrieved from Li/Li coin cells after 20, 100, and 250 h of cycling at 1 mA cm^{-2} and 1 mAh cm^{-2} (samples prepared with 1:24 dilution in diglyme to enable measurements). While the ^7Li spectrum shows a downfield shift, similar to that observed for the 2.4LN-0LB electrolyte (Figure S16a), the peak corresponding to BOB^- (159.4 ppm) is absent in the ^{13}C spectrum of the cycled electrolyte (Figure S17). In comparison, the ^7Li NMR spectrum of the 1.2LN-1.2LB electrolyte post 250 h shows a minor upfield shift instead (Figure S16b), while the ^{13}C postcycling spectrum indicates the presence of BOB^- after 250 h (Figure S18). Moreover, the BOB^- concentration only shows a modest drop going from hour 100 to hour 250, suggesting that the BOB^- consumption decreases after Li surface stabilization. We also analyzed Li plating/stripping in Li/Cu cells with "0LN-1.2LB" (i.e., no $LiNO_3$) composition (Figure S19). Not only does the absence of $LiNO_3$ result in much lower CEs per cycle (46.6% and lower) but also a different more sloping voltage profile for stripping (Figure S19b). With cycling, while no significant changes to the ohmic drop occur, the stripping voltage trace further diverges, with the CE eventually dropping to 0%. Therefore, while the presence of $LiNO_3$ seems critical in achieving high CE per cycle, the presence of BOB^- in sufficient amounts appears key to extending the cycle life, as evidenced by the stable Li plating/stripping voltage traces for the 1.2LN-1.2LB electrolyte. Clearly, the improvements in the Li interface stability in $LiNO_3$/LiBOB/diglyme electrolytes are highly synergistic in nature.

We performed electrochemical impedance spectroscopy (EIS) to track the evolution of the bulk electrolyte and Li interface resistances with cycling (Nyquist plots shown in Figure 4h–j, zoomed-in insets of the high-frequency points shown in Figure S20). The resulting bulk electrolyte resistance (taken from the high-frequency real axis intercept) and total interface resistance (taken as the difference between the high- and low-frequency real axis intercepts), R_E and R_{TI}, respectively, are provided in Table S3. Comparing the Nyquist plots right after formation cycling (0.1 mA cm^{-2} and 4 mAh cm^{-2}), it is observed that the 2.4LN-0LB electrolyte has the highest R_{TI} and the 2LN-0.4LB the lowest, in line with the j_{ex}^P trends (Figure 4a). R_E also follows the same trend as with the bulk ionic conductivity measurements (Figure 1a), with the 1.2LN-1.2LB electrolyte having the lowest R_E (5.6 $\Omega.cm^2$). With cycling, R_{TI} drops for all of the electrolytes, likely due to improved SEI passivation and the Li surface area increase; however, R_E also increases, likely due to Li^+ consumption from the electrolyte. For the 2.4LN-0LB electrolyte, the R_E increase is the most severe (14.5 to 31.8 Ω cm^2 after 50 cycles), and an additional semicircle also appears at high frequencies (10^7 to 10^5 Hz). For the 2M-0.4M electrolyte, while there is a significant reduction in R_{TI} after 50 cycles, both a significant R_E increase and an additional high-frequency semicircle are observed after 150 cycles. The distribution of relaxation time (DRT) analysis of the EIS spectra (Figure S21) also shows the presence of additional features at high frequencies for these spectra. Here, the narrow peak at high frequencies ($\tau = 10^{-8}$ to 10^{-6} s) could correspond to the increased contact resistance at the Li/current collector interface induced by uneven Li deposition, while the broader feature at slightly lower frequencies ($\tau = 10^{-6}$ to 10^{-5} s) could indicate (partially) electronically conducting organic decomposition layers on Li. In contrast, the R_E barely changes for the 1.2LN-1.2LB electrolyte (2.5−3 Ω after 50 cycles) and R_{TI} also stays nearly the same between 50 and 150 cycles without the emergence of additional features. Clearly, the presence of LiBOB seems to have a profound effect on retaining the ionic conductivity and stabilizing the Li−electrolyte interface.

SEI Composition and Li Microstructure. The electrochemical results suggest that the improvements in (electro)-chemical stability for the F-free electrolytes with the inclusion of LiBOB are linked to changes in characteristics of the Li/electrolyte interface, which could be in terms of both the Li deposition morphology and SEI composition. In Li metal batteries, Li inventory loss can occur due to both (continuous) SEI and dead Li formation. Here, we employ operando ^7Li NMR to understand the evolution of the Li plating morphology with cycling and to determine the fraction of Li inventory lost to SEI and dead Li.[49] ^7Li NMR is sensitive to different Li morphologies depending on their orientation with respect to the static magnetic field B_0 and can vary between 240 and 275 ppm. While planar Li (Figure 5a, right) with a perpendicular orientation to B_0 corresponds to around 240 ppm, chemical shifts in the range of 270−275 ppm are typically reported for dendritic Li deposits (Figure 5a, left) having a parallel orientation to B_0.[49] Besides these, deposits with intermediate orientations or mossy deposits result in intermediate chemical shift values (Figure 5a, middle).[50] It is also important to consider the bulk magnetic susceptibility (BMS) effects of the counter electrode while interpreting the chemical shifts, as paramagnetic electrodes such as $LiFePO_4$ (LFP) could result in a downfield shift of about 15 ppm for metallic Li peaks.[49] For instance, the chemical shift for planar Li, around 240−245 ppm in Li/Li or Li/Cu cells, would be around 255−260 ppm in Cu/LFP cells.

The evolution of the Li morphology in Cu/LFP cells cycled for 4 cycles at 0.5 mA cm^{-2} and 0.5 mAh cm^{-2} (1 h) plating per cycle is shown in Figure 5b, and the breakdown of Li utilization per cycle (based on the methodology proposed by Gunnarsdóttir et al.,[49] more details provided under Supplementary Note 2) is shown in Figure 5c. For the 2.4LN-0LB electrolyte, the metallic ^7Li signal initially has a chemical shift of around 256 ppm, with a shoulder feature around 270 ppm. With further cycling, a gradual shift of overall peak intensity to ∼272 ppm is observed (Figure S22), clearly suggesting a transition in the Li deposition morphology. The remaining dead Li peak after 4 cycles has a chemical shift of ∼284 ppm, suggesting the formation of dendrites. The Li loss toward dead Li formation also progressively increases from cycle 2 to cycle 4 (Figure 5c). The 2LN-0.4LB electrolyte shows much higher reversible Li plating, with the metallic Li peak consistently centered around ∼256−258 ppm, indicating uniform deposition, and the Li loss is predominantly toward SEI formation (rather than dead Li, as confirmed by the postdischarge spectra shown in Figure S22). Similar amounts of reversible and lost Li

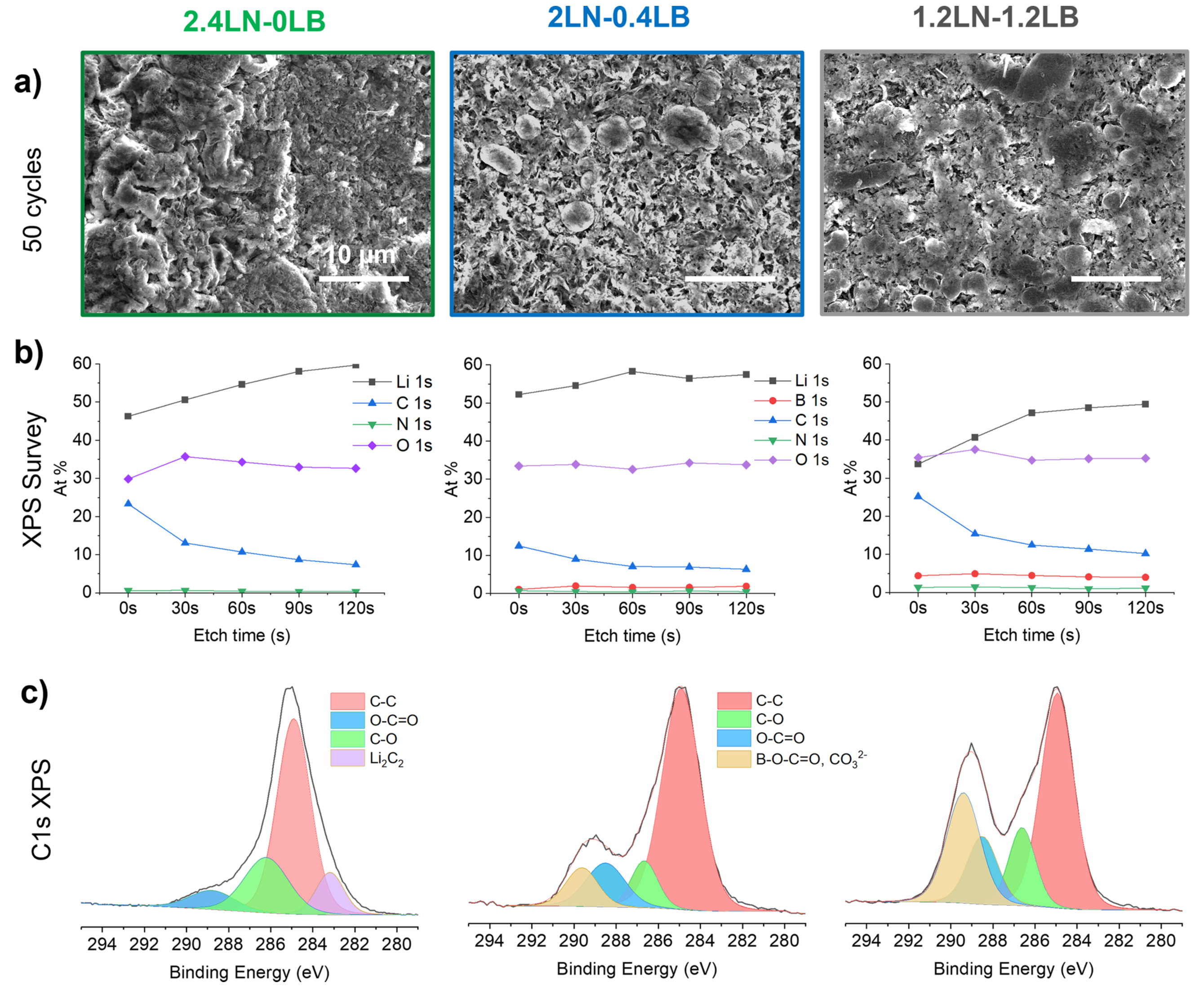

Figure 6. Li morphology and interphase composition after 50 cycles in Li/Cu cells at 1 mA cm^{-2} and 1 mAh cm^{-2}: (a) SEM images of 2.4LN-0LB, 2LN-0.4LB, and 1.2LN-1.2LB samples. The scale bar is 10 μm. (b) XPS survey atomic percentage (with depth profiling) for 2.4LN-0LB, 2LN-0.4LB, and 1.2LN-1.2LB samples. (c) C 1s XPS spectra of 2.4LN-0LB, 2LN-0.4LB, and 1.2LN-1.2LB samples.

are also observed for the 1.2LN-1.2LB electrolyte, but the metallic Li peak, initially around 262 ppm, becomes centered around 270 ppm with subsequent cycling.

These trends are also reflected in the top-view SEM images of 1 mAh cm^{-2} electrodeposited Li on Cu after the first and fifth deposition half cycles (Figure 5d and Figure S23); the 2.4LN-0LB electrolyte shows a mix of planar and mossy deposits after the first cycle, while a mix of dendritic and planar deposits is observed after 5 cycles. This suggests that the transition of mossy Li to dendritic Li could have resulted in the overall downfield shift of the ^{7}Li metallic peak between cycles 1−4. The 2LN-0.4LB electrolyte shows even, closely packed, high-surface-area features, forming larger, planar deposits after the first cycle. These features appear to coalesce further after 5 cycles, but the surface features and the overall morphology remain nearly the same. In comparison, the 1.2LN-1.2LB electrolyte shows larger Li grains with a curved orientation after the first cycle. Upon further cycling, larger disk-like deposits are observed (Figure S23). The corresponding operando NMR ^{7}Li chemical shift of ~270 ppm, likely originating from the curved surface orientation of these deposits, is consistent with previous results for similar Li morphologies obtained in Cu/LFP cells.[51]

With subsequent cycling, the Li surface morphology undergoes significant changes. Figure 6a shows the SEM top view of the electrodeposited Li surface after 50 cycles at 1 mA cm^{-2} and 1 mAh cm^{-2}, and Figures 6b and 7c show the corresponding survey and C 1s XPS compositions of the surfaces, respectively. For the 2.4LN-0LB electrolyte, the Li deposition is significantly uneven, with the formation of a surface layer on top. The corresponding XPS survey spectrum shows a high concentration of C at the surface that decreases with etching, along with an increase in Li and O concentrations. In the high-resolution C 1s spectrum (Figure 6c), in addition to the adventitious C−C carbon peak at 284.8 eV, another significant environment is observed at 286.8 eV, which could correspond to Li alkoxides (R−CO−Li) typically known to form with ether decomposition at the Li surface.[52] This possibility is also supported by the O 1s spectrum (Figure S24), where a significant peak is observed in the region corresponding to alkoxides (~531 eV), alongside Li_2O (~528 eV), formed upon $LiNO_3$ reduction.[27] An environment is also

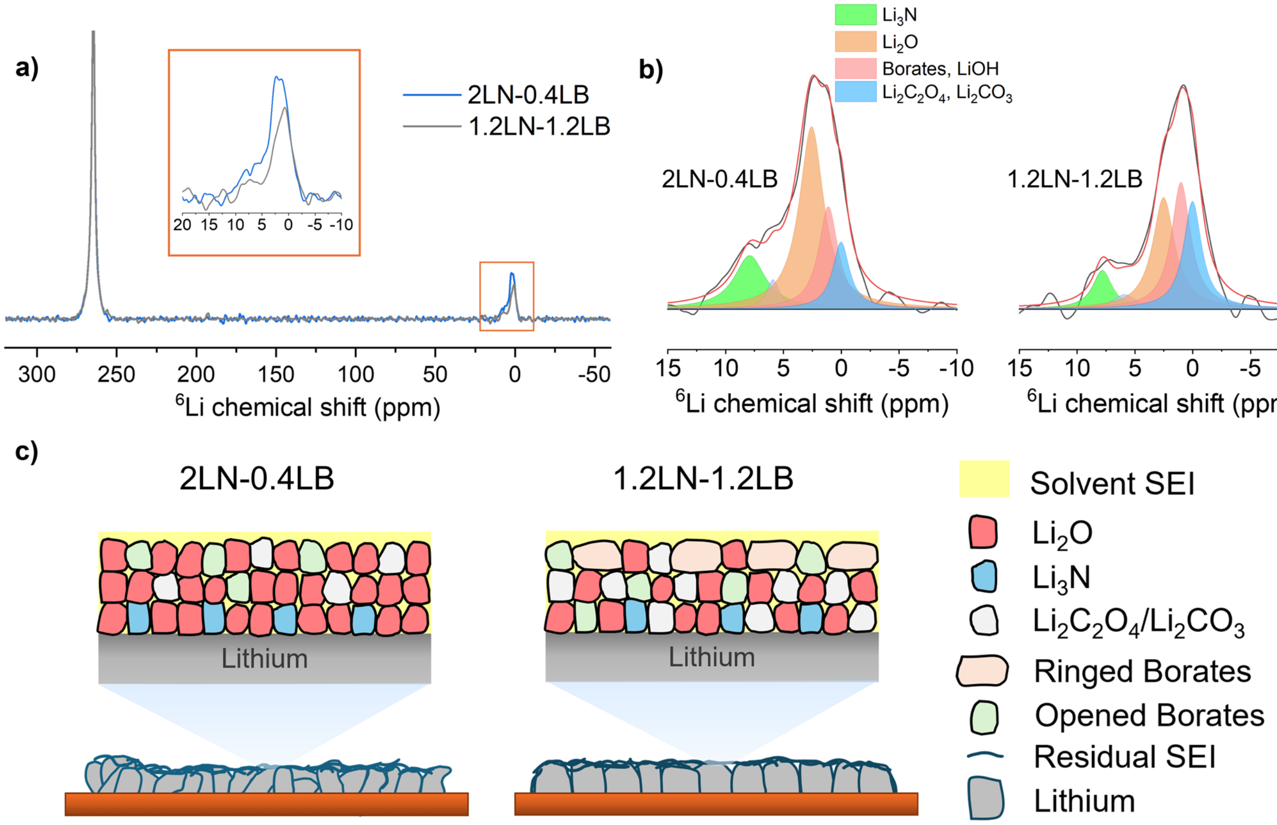

Figure 7. (a) ^{6}Li MAS NMR of the SEI after 440 cycles in Li/Cu cells at 0.5 mA cm^{-2} and 1 mAh cm^{-2} normalized to the intensity of dead Li. (b) ^{6}Li NMR diamagnetic (SEI) region of 2LN-0.4LB and 1.2LN-1.2LB samples with fits. (c) Schematic diagram highlighting the differences in the electrodeposited Li morphology and SEI structure for 2LN-0.4LB and 1.2LN-1.2LB electrolytes.

observed at 283 eV, which could correspond to Li_2C_2, which is formed upon further reduction of organic SEI components on lithium, and is known to be electronically conductive.[53] This might also explain the additional high-frequency semicircle in the EIS post-50 cycles (Figure 4h).

In contrast, the 2LN-0.4LB and 1.2LN-1.2LB electrolytes show a more uniform Li surface morphology, where the Li deposits are surrounded or covered by a scaffold-like structure. For the 2LN-0.4LB electrolyte, this structure appears porous, whereas for the 1.2LN-1.2LB electrolyte, this structure appears more compact. The chemical compositions of these surfaces are also different. The 2LN-0.4LB electrolyte results in a much lower C content throughout the SEI, with Li and O dominating the SEI composition (Figure 6b). The C 1s spectrum (Figure 6c) reveals a relative increase in the O−C═O peak at 288.5 eV, which could be due to the presence of $Li_2C_2O_4$,[54] and the emergence of a new environment around 289.5 eV, which could correspond to overlapping features such as borates formed upon LiBOB reduction with Li traces of LiBOB and Li_2CO_3.[54−56] In the O 1s spectrum (Figure S24) at the top surface, a dominant contribution from Li_2O (528.5 eV) is observed, alongside Li alkoxides/LiOH (~531 eV) and a new environment at 531.5 eV corresponding to C═O derivatives from LiBOB and Li_2CO_3.[57] The presence of LiBOB derivatives in the SEI is further confirmed by B 1s XPS (Figure S25), where a peak is observed at lower binding energies (~191 eV) than that for the BOB^- anion (193.7 eV), which could correspond to 3-coordinate boron decomposition products of LiBOB.[55]

For the 1.2LN-1.2LB electrolyte, the top surface of the SEI shows a high C content, and this value continues to be marginally higher compared with that of the 2.4LN-0LB electrolyte (Figure 6b) with etching. Furthermore, the relatively lower Li content in the outer SEI layers (0−30 s etching) and an increased presence of B (4−5 at %) suggest that these outer SEI layers could be primarily made up of LiBOB derivatives. The C 1s spectrum (Figure 6c) reveals a strong increased amount of B−O−C═O/Li_2CO_3 (289.5 eV) in the SEI. In the O 1s spectrum, the C═O/Li_2CO_3 peak is now the most dominant, with an additional peak at 532.5 eV, which could correspond to the bridging oxygen (B−O−C) of less reduced intermediates of LiBOB. The B 1s XPS spectrum also indicates a less reduced environment on the outer SEI layers (~192 eV) covering the more reduced LiBOB derivatives at ~191 eV (Figure S25). These environments likely correspond to 3-coordinate ringed oxalatoborates (having one oxalatoborate ring intact) and fully ring-opened borates, respectively, known to form upon the stepwise reduction of LiBOB.[55,58] This also suggests that the increase in the 289.5 eV peak in C 1s XPS primarily originates from these environments (Figure 6c).

While it is challenging to obtain a quantitative estimate of changes to the Li surface area with cycling, cyclic voltammetry has previously been used to track the increase in the active surface area in Li/Li and Li/Cu cells.[45] The cyclic voltammograms of Li/Cu cells with fluorine-free electrolytes (scan rate = 1 mV s^{-1}) are shown in Figure S26a−c, and the anodic peak integral per scan as a correlated descriptor for the electrochemically active Li surface area (with minor contributions to

https://doi.org/10.1021/jacs.5c12584

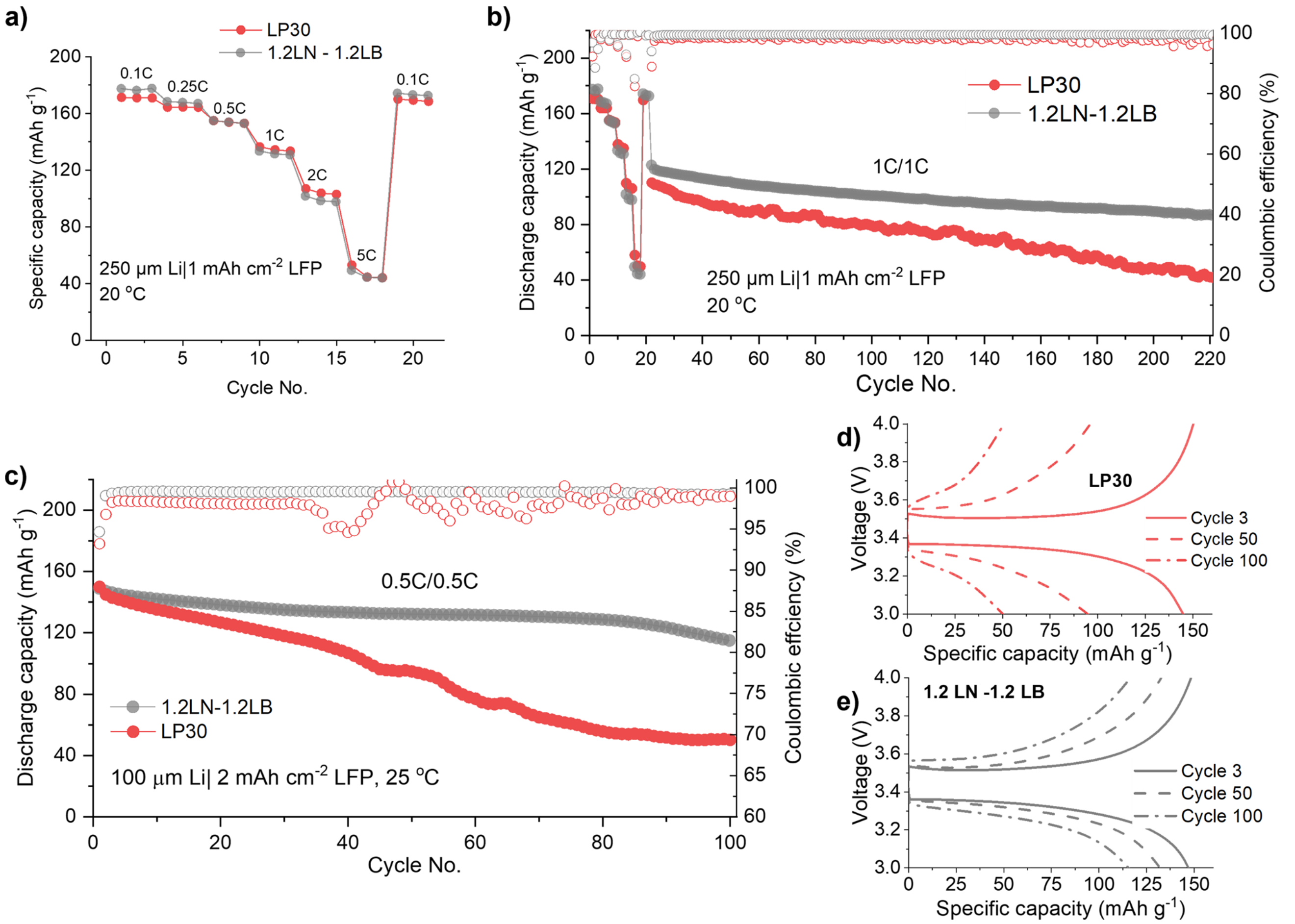

Figure 8. (a) Rate performances of Li/LFP (1 mAh cm^{-2}) half-cells at varying charge/discharge rates at 20 °C. (b) Discharge capacities and Coulombic efficiencies for the Li/LFP (1 mAh cm^{-2}) half-cells with extended cycling at 1C for 200 cycles at 20 °C. (c) Discharge capacities and Coulombic efficiencies in Li/LFP (2 mAh cm^{-2}) full cells with LP30 and 1.2LN-1.2LB electrolytes at 25 °C. (d) Voltage traces for the LP30 Li/LFP cells at 3, 50, and 100 cycles. (e) Voltage traces for the 1.2LN-1.2LB Li/LFP cells at 3, 50, and 100 cycles.

the integral from transport polarization and SEI redox) is provided in Figure S26d. Here, we observe that for the 2.4LN-0LB electrolyte, the anodic peak integral is low and does not significantly change with cycling. In contrast, the anodic peak integral continuously increases for the 2LN-0.4LB electrolytes. In high-CE electrolytes, such an increase in exchange current (and thereby the anodic integral) is typically associated with an increase in the Li active surface area. Here, however, this increase is exponential, particularly after cycle 5. At this stage, the anodic peak also turns noisy, which can be attributed to the mechanical/electronic disconnection of the Li/SEI network from the current collector during stripping at these high current densities. This is also evident from the SEM images of the Cu current collector after 11 CV scans (Figure S27, left) where the residual Li/SEI on the Cu surface appears porous and highly pitted. In contrast, the 1.2LN-1.2LB electrolyte results in a steady rise in the peak anodic integral, which stabilizes after about 25 cycles. The SEM images after 11 CV scans (Figure S27, right) also show a much smoother Li/SEI residue on Cu. This implies that while both 2LN-0.4LB and 1.2LN-1.2LB electrolytes display high CEs, the higher active surface area of electrodeposited Li for the 2LN-0.4LB electrolyte, as suggested by SEM, CV, and operando NMR, results in overall higher Li$^+$/anion consumption, leading to accelerated Li$^+$/anion depletion.

A further validation of our hypothesis on SEI composition and the overall amount of Li in the SEI relative to the amount of Li deposits is achieved using naturally abundant ^{6}Li solid-state NMR (ssNMR). We complement this with cross-sectional SEM to obtain a visual estimate of the overall dead Li/SEI residue generated. Here, we used Li/SEI residues on Cu foils after 440 cycles at 0.5 mA cm^{-2} and 1 mAh cm^{-2} for the experiments. ^{6}Li was chosen over ^{7}Li NMR to obtain a better chemical shift resolution on the SEI components.

The postcycling cross-sectional SEM images (Figure S28) reveal that the amount of dead Li/SEI residue generated after 440 cycles is nearly the same (around 64.5 µm) for the 2LN-0.4LB and 1.2LN-1.2LB electrolytes. Another factor to be considered here is the skin depth for ^{6}Li, which could impact rf penetration into metallic Li, resulting in its nonuniform excitation. While the skin depth for ^{6}Li for a Larmor frequency of 73.6 MHz (on a 11.7 T magnet) is around 18 µm (see Supplementary Note 3), the size of Li deposits in the Li/SEI residue was observed to be <10 µm for both the electrolytes (Figure S28, highlighted circles), much smaller than the ^{6}Li skin depth. Furthermore, the sinusoidal shape of the ^{6}Li nutation curve obtained for metallic Li from the prepared Li/SEI sample (Figure S29) indicates that all metallic Li in the sample is uniformly excited by the rf signal. These findings validate our choice of ^{6}Li NMR spectra normalization with respect to the dead Li peak at ∼260 ppm for the sake of comparison (Figure 7a). With this approach, we observe that the 2LN-0.4LB electrolyte has a relatively higher area of the diamagnetic peak at ∼0 ppm, corresponding to Li-containing SEI components (Figure 7a, zoomed inset). The compositions of SEI are also different (Figure 7b). Li_2O at ∼2.6 ppm is the dominant SEI component for the 2LN-0.4LB electrolyte,[59] with minor peaks at ∼1 ppm, 0 ppm (corresponding to $Li_2C_2O_4/Li_2CO_3$),[60] and ∼7.5 ppm (corresponding to Li_3N).[61,62] While the peak at ∼1 ppm could correspond to LiOH (due to Li reactivity with moisture traces),[59] we believe that this peak also includes contributions from borate intermediates from LiBOB decomposition. This is plausible, as pristine LiBOB salt has a chemical shift of ∼0.3 ppm (Figure S30), and (partial) ring-opened anions would result in deshielding of Li and a higher chemical shift. For the 1.2LN-1.2LB electrolyte, the ratio of Li-borate/LiOH and $Li_2C_2O_4/Li_2CO_3$ peaks increases, with reduced contributions from Li_2O and Li_3N. These observations corroborate the C 1s, O 1s, and B 1s XPS results, which also indicated the existence of multiple LiBOB-derived environments for the 1.2LN-1.2LB electrolyte.

Summarizing, the addition of LiBOB into $LiNO_3$/diglyme electrolytes improves Li plating/stripping in terms of both homogenizing Li deposition at high current densities and lowering Li^+/anion consumption from the electrolyte with cycling. While the addition of LiBOB as a minor secondary salt already improves Li^+ dissociation, leading to homogeneous Li plating/stripping with high CE, the surface area of Li deposits remains high, leading to Li^+/anion consumption-induced cell failure. On increasing the LiBOB concentration further, the initial and subsequent Li deposition turns out to be more compact (lower surface area). This highlights the beneficial role of organoboron derivatives in the outer SEI in tuning the Li deposition size. Our results also suggest that the SEI scaffold formed with mainly $LiNO_3$-derived SEI components does not provide adequate mechanical passivation of fresh Li deposits with subsequent cycling or at high currents, while LiBOB-derived borates have been previously reported to chemo-mechanically passivate the Li metal surface,[56] and our postmortem analyses suggest that a similar mechanism could be at play for the fluorine-free electrolytes. The reduction in surface area evolution of Li deposits results in lower overall Li^+/anion consumption from the electrolyte toward SEI formation during cycling (Figure 7c). It is to be noted, however, that the inner SEI, predominantly made up of Li_2O, is essential in ensuring high Li^+ conductivity in the SEI and chemical passivation of Li, highlighting the synergistic roles of $LiNO_3$ and LiBOB in improving the SEI properties.

Electrochemical Performance in Lithium Metal Batteries. We further demonstrate the practical applicability of the fluorine-free 1.2LN-1.2LB electrolyte by evaluating its electrochemical performance in half and full cells. The linear sweep voltammetry (LSV) measurements performed in Li/stainless-steel cells at 0.1 mV s^{-1} at 25 °C (Figure S31) indicate that the anodic stability of fluorine-free electrolytes slightly improves with the inclusion of LiBOB, similar to a previous report.[26] The 1.2LN-1.2LB electrolyte shows much lower leakage currents compared to the electrolytes with lower amounts of LiBOB and displays an electrochemical stability of up to 4.3 V vs Li^+/Li, rendering it suitable for LMB applications with $LiFePO_4$ (LFP) as the cathode material.

At 20 °C, the rate performances of 1.2LN-1.2LB and LP30 electrolytes in Li/LFP half-cells with commercial 1 mAh cm^{-2} LFP cathodes (Figure 8a) are very similar (176 mAh g^{-1} vs 171 mAh g^{-1} at 0.1C and 44.24 mAh g^{-1} vs 44.6 mAh g^{-1} at 5C for 1.2LN-1.2LB and LP30, respectively). However, with continued cycling at 1C for another 200 cycles (Figure 8b), the LP30 electrolyte undergoes a rapid capacity fade due to high-current-induced Li surface degradation. On the other hand, the 1.2LN-1.2LB electrolyte continues to display stable cycling with an average Coulombic efficiency of 99.5% over the 200 cycles (versus 98.5% for LP30). Under more realistic full-cell conditions, i.e., with a low lithium reservoir of 100 μm and LFP cathodes with an active mass loading of 2 mAh cm^{-2} and at 25 °C (Figure 8c), the 1.2LN-1.2LB electrolyte significantly outperforms LP30 with a capacity retention of 77.2%, an average discharge capacity of 132.36 mAh g^{-1}, and an average Coulombic efficiency of 99.4% (versus a capacity retention of 33.5%, an average discharge capacity of 92.47 mAh g^{-1}, and an average Coulombic efficiency of 98.1% for LP30) after 100 cycles at 0.5C charge and discharge. From the voltage traces shown for cycles 3, 50, and 100 (Figure 8d,e), it is observed that the 1.2LN-1.2LB electrolyte has both a lower ohmic drop and a less sloping charge/discharge voltage profile (i.e., lower concentration polarization) with extended cycling. The capacity retention increases to 86.7% after 100 cycles and 68.9% after 150 cycles with an improved CE of 99.65% using an asymmetric charge/discharge protocol (0.2C charge, 0.5C discharge, Figure S32). While further solvent optimization is necessary to further extend the applicability of these electrolytes to LMBs with high-voltage (>4 V) cathodes, we believe that these results mark an important step forward in the design of safe, fluorine-free electrolytes for LMBs.

CONCLUSIONS

In this work, we demonstrate how the modification of Li^+ inner solvation structures using a dual-salt approach, and its consequent influence on Li^+ transport and SEI composition, could hold the key to achieving stable Li plating/stripping in fluorine-free electrolytes. Our combined experimental and computational approach, used to elucidate the mechanistic changes to ion transport upon the introduction of LiBOB into $LiNO_3$/diglyme electrolytes, reveals that LiBOB's steric bulk and participation in the inner solvation sheath reduce the extent of $Li^+{-}NO_3^-$ pairing, increasing ion dissociation and increasing the diversity of solvation structures. This leads to an increase in ionic conductivity despite a drop in bulk transport properties such as viscosity and self-diffusivity. Simultaneously, this increased $Li^+{-}BOB^-$ coordination also results in the formation of LiBOB-derived outer SEI components over the ion-conductive, $LiNO_3$-derived, Li_2O/Li_3N-rich inner SEI layer, as identified by the XPS and solid-state NMR analyses. Our early-stage morphological analyses through operando NMR and SEM also indicate that these synergistic improvements to charge carrier concentration and SEI composition enable uniform Li nucleation and deposition from the onset, resulting in larger (lower surface area) Li deposits and lower Li^+/anion consumption into the SEI, contributing to a significantly improved cycling stability.

By outlining the specific contributions of the two readily available fluorine-free salts, $LiNO_3$ and LiBOB, to ion transport properties and SEI/Li morphology structure, we propose a dual-salt pathway for future fluorine-free electrolyte development, where organoboron salts such as LiBOB could play a major role as functional alternatives to fluorinated additives, while $LiNO_3$ contributes toward the formation of an ion-conductive inner SEI. These insights could accelerate advancement in fluorine-free electrolyte systems, opening a clearer path toward safe, sustainable next-generation lithium batteries.

■ ASSOCIATED CONTENT

Supporting Information

The Supporting Information is available free of charge at https://pubs.acs.org/doi/10.1021/jacs.5c12584.

> Experimental details; calculation methodologies; PFG-NMR; CV; LSV; additional rheometry, conductivity, NMR, Raman analysis, MD, electrochemical performance, XPS, and SEM data (PDF)

■ AUTHOR INFORMATION

Corresponding Author

Fokko M. Mulder − *Department of Chemical Engineering, Faculty of Applied Sciences, Delft University of Technology, Delft 2629HZ, The Netherlands;* orcid.org/0000-0003-0526-7081; Email: F.m.mulder@tudelft.nl

Authors

Pranav Karanth − *Department of Chemical Engineering, Faculty of Applied Sciences, Delft University of Technology, Delft 2629HZ, The Netherlands; Department of Radiation Science and Technology, Faculty of Applied Sciences, Delft University of Technology, Delft 2629JB, The Netherlands;* orcid.org/0000-0002-9945-2845

Mark Weijers − *Department of Chemical Engineering, Faculty of Applied Sciences, Delft University of Technology, Delft 2629HZ, The Netherlands;* orcid.org/0000-0002-8678-7355

Anastasia K. Lavrinenko − *Department of Radiation Science and Technology, Faculty of Applied Sciences, Delft University of Technology, Delft 2629JB, The Netherlands;* orcid.org/0000-0001-9863-8325

Boaz Izelaar − *Department of Process and Energy, Faculty of Mechanical Engineering, Delft University of Technology, Delft 2628CB, The Netherlands;* orcid.org/0000-0002-2923-907X

Ruud Kortlever − *Department of Process and Energy, Faculty of Mechanical Engineering and e-Refinery Institute, Delft University of Technology, Delft 2628CB, The Netherlands;* orcid.org/0000-0001-9412-7480

Swapna Ganapathy − *Department of Radiation Science and Technology, Faculty of Applied Sciences, Delft University of Technology, Delft 2629JB, The Netherlands;* orcid.org/0000-0001-5265-1663

Marnix Wagemaker − *Department of Radiation Science and Technology, Faculty of Applied Sciences, Delft University of Technology, Delft 2629JB, The Netherlands;* orcid.org/0000-0003-3851-1044

Complete contact information is available at: https://pubs.acs.org/10.1021/jacs.5c12584

Author Contributions

The manuscript was written through the contributions of all authors. All authors have given approval to the final version of the manuscript.

Notes

The authors declare no competing financial interest.

■ ACKNOWLEDGMENTS

This project has received funding from the European Union's Horizon 2020 research and innovation program under grant agreement no. 875557. Neither the European Commission nor any person acting on behalf of the Commission is responsible for how the following information is used. The views expressed in this publication are the sole responsibility of the authors and do not necessarily reflect the views of the European Commission. The authors would like to thank Bart Boshuizen and Stephen Eustace for their assistance with the experiments.

■ REFERENCES

(1) Liu, J.; Bao, Z.; Cui, Y.; Dufek, E. J.; Goodenough, J. B.; Khalifah, P.; Li, Q.; Liaw, B. Y.; Liu, P.; Manthiram, A.; Meng, Y. S.; Subramanian, V. R.; Toney, M. F.; Viswanathan, V. V.; Whittingham, M. S.; Xiao, J.; Xu, W.; Yang, J.; Yang, X.-Q.; Zhang, J.-G. Pathways for Practical High-Energy Long-Cycling Lithium Metal Batteries. *Nat. Energy* **2019**, *4* (3), 180−186.

(2) Lin, D.; Liu, Y.; Cui, Y. Reviving the Lithium Metal Anode for High-Energy Batteries. *Nat. Nanotechnol.* **2017**, *12* (3), 194−206.

(3) Cheng, X.-B.; Zhang, R.; Zhao, C.-Z.; Zhang, Q. Toward Safe Lithium Metal Anode in Rechargeable Batteries: A Review. *Chem. Rev.* **2017**, *117* (15), 10403−10473.

(4) Qian, J.; Henderson, W. A.; Xu, W.; Bhattacharya, P.; Engelhard, M.; Borodin, O.; Zhang, J.-G. High Rate and Stable Cycling of Lithium Metal Anode. *Nat. Commun.* **2015**, *6* (1), 6362.

(5) Su, C.-C.; He, M.; Amine, R.; Rojas, T.; Cheng, L.; Ngo, A. T.; Amine, K. Solvating Power Series of Electrolyte Solvents for Lithium Batteries. *Energy Environ. Sci.* **2019**, *12* (4), 1249−1254.

(6) Weber, R.; Genovese, M.; Louli, A. J.; Hames, S.; Martin, C.; Hill, I. G.; Dahn, J. R. Long Cycle Life and Dendrite-Free Lithium Morphology in Anode-Free Lithium Pouch Cells Enabled by a Dual-Salt Liquid Electrolyte. *Nat. Energy* **2019**, *4* (8), 683−689.

(7) Wang, Q.; Zhao, C.; Wang, S.; Wang, J.; Wu, F.; Ombrini, P.; Ganapathy, S.; Eustace, S.; Bai, X.; Li, B.; Armand, M.; Aurbach, D.; Wagemaker, M. Interphase Design for Lithium-Metal Anodes. *J. Am. Chem. Soc.* **2025**, *147* (11), 9365−9377.

(8) Yu, Z.; Wang, H.; Kong, X.; Huang, W.; Tsao, Y.; Mackanic, D. G.; Wang, K.; Wang, X.; Huang, W.; Choudhury, S.; Zheng, Y.; Amanchukwu, C. V.; Hung, S. T.; Ma, Y.; Lomeli, E. G.; Qin, J.; Cui, Y.; Bao, Z. Molecular Design for Electrolyte Solvents Enabling Energy-Dense and Long-Cycling Lithium Metal Batteries. *Nat. Energy* **2020**, *5* (7), 526−533.

(9) Yu, Z.; Rudnicki, P. E.; Zhang, Z.; Huang, Z.; Celik, H.; Oyakhire, S. T.; Chen, Y.; Kong, X.; Kim, S. C.; Xiao, X.; Wang, H.; Zheng, Y.; Kamat, G. A.; Kim, M. S.; Bent, S. F.; Qin, J.; Cui, Y.; Bao, Z. Rational Solvent Molecule Tuning for High-Performance Lithium Metal Battery Electrolytes. *Nat. Energy* **2022**, *7* (1), 94−106.

(10) Cao, X.; Jia, H.; Xu, W.; Zhang, J.-G. Review—Localized High-Concentration Electrolytes for Lithium Batteries. *J. Electrochem. Soc.* **2021**, *168* (1), No. 010522.

(11) Cao, X.; Ren, X.; Zou, L.; Engelhard, M. H.; Huang, W.; Wang, H.; Matthews, B. E.; Lee, H.; Niu, C.; Arey, B. W.; Cui, Y.; Wang, C.; Xiao, J.; Liu, J.; Xu, W.; Zhang, J.-G. Monolithic Solid-Electrolyte Interphases Formed in Fluorinated Orthoformate-Based Electrolytes Minimize Li Depletion and Pulverization. *Nat. Energy* **2019**, *4* (9), 796−805.

(12) Chen, S.; Zheng, J.; Yu, L.; Ren, X.; Engelhard, M. H.; Niu, C.; Lee, H.; Xu, W.; Xiao, J.; Liu, J.; Zhang, J.-G. High-Efficiency Lithium Metal Batteries with Fire-Retardant Electrolytes. *Joule* **2018**, *2* (8), 1548−1558.

(13) Yu, L.; Chen, S.; Lee, H.; Zhang, L.; Engelhard, M. H.; Li, Q.; Jiao, S.; Liu, J.; Xu, W.; Zhang, J.-G. A Localized High-Concentration Electrolyte with Optimized Solvents and Lithium Difluoro(Oxalate)-Borate Additive for Stable Lithium Metal Batteries. *ACS Energy Lett.* **2018**, *3* (9), 2059−2067.

(14) National Institute of Environmental Health Sciences. *Perfluoroalkyl and Polyfluoroalkyl Substances (PFAS)*. https://www.niehs.nih.gov/health/topics/agents/pfc (accessed 2024–08–23).

(15) Fenton, S. E.; Ducatman, A.; Boobis, A.; DeWitt, J. C.; Lau, C.; Ng, C.; Smith, J. S.; Roberts, S. M. Per- and Polyfluoroalkyl Substance Toxicity and Human Health Review: Current State of Knowledge and Strategies for Informing Future Research. *Environ. Toxicol. Chem.* **2020**, *40* (3), 606–630.

(16) Vieira, V. M.; Hoffman, K.; Shin, H.-M.; Weinberg, J. M.; Webster, T. F.; Fletcher, T. Perfluorooctanoic Acid Exposure and Cancer Outcomes in a Contaminated Community: A Geographic Analysis. *Environ. Health Perspect.* **2013**, *121* (3), 318–323.

(17) ECHA. *Registry of restriction intentions until outcome*. https://echa.europa.eu/registry-of-restriction-intentions/-/dislist/details/0b0236e18663449b (accessed 2024–08–23).

(18) Larsson, F.; Andersson, P.; Blomqvist, P.; Mellander, B.-E. Toxic Fluoride Gas Emissions from Lithium-Ion Battery Fires. *Sci. Rep.* **2017**, *7* (1), 10018.

(19) Huang, W.; Wang, H.; Boyle, D. T.; Li, Y.; Cui, Y. Resolving Nanoscopic and Mesoscopic Heterogeneity of Fluorinated Species in Battery Solid-Electrolyte Interphases by Cryogenic Electron Microscopy. *ACS Energy Lett.* **2020**, *5* (4), 1128–1135.

(20) Surace, Y.; Leanza, D.; Mirolo, M.; Kondracki, Ł.; Vaz, C. A. F.; El Kazzi, M.; Novák, P.; Trabesinger, S. Evidence for Stepwise Formation of Solid Electrolyte Interphase in a Li-Ion Battery. *Energy Storage Mater.* **2022**, *44*, 156–167.

(21) Guo, R.; Gallant, B. M. Li2O Solid Electrolyte Interphase: Probing Transport Properties at the Chemical Potential of Lithium. *Chem. Mater.* **2020**, *32* (13), 5525–5533.

(22) Hobold, G. M.; Wang, C.; Steinberg, K.; Li, Y.; Gallant, B. M. High Lithium Oxide Prevalence in the Lithium Solid-Electrolyte Interphase for High Coulombic Efficiency. *Nat. Energy* **2024**, *9* (5), 580–591.

(23) May, R.; Fritzsching, K. J.; Livitz, D.; Denny, S. R.; Marbella, L. E. Rapid Interfacial Exchange of Li Ions Dictates High Coulombic Efficiency in Li Metal Anodes. *ACS Energy Lett.* **2021**, *6* (4), 1162–1169.

(24) Chen, H.; Chen, K.; Luo, L.; Liu, X.; Wang, Z.; Zhao, A.; Li, H.; Ai, X.; Fang, Y.; Cao, Y. LiNO3-Based Electrolytes via Electron-Donation Modulation for Sustainable Nonaqueous Lithium Rechargeable Batteries. *Angew. Chem., Int. Ed.* **2024**, *63* (10), No. e202316966.

(25) Wang, Q.; Zhao, C.; Yao, Z.; Wang, J.; Wu, F.; Kumar, S. G. H.; Ganapathy, S.; Eustace, S.; Bai, X.; Li, B.; Lu, J.; Wagemaker, M. Entropy-Driven Liquid Electrolytes for Lithium Batteries. *Adv. Mater.* **2023**, *35* (17), No. 2210677.

(26) Choudhury, S.; Tu, Z.; Nijamudheen, A.; Zachman, M. J.; Stalin, S.; Deng, Y.; Zhao, Q.; Vu, D.; Kourkoutis, L. F.; Mendoza-Cortes, J. L.; Archer, L. A. Stabilizing Polymer Electrolytes in High-Voltage Lithium Batteries. *Nat. Commun.* **2019**, *10* (1), 3091.

(27) Adams, B. D.; Carino, E. V.; Connell, J. G.; Han, K. S.; Cao, R.; Chen, J.; Zheng, J.; Li, Q.; Mueller, K. T.; Henderson, W. A.; Zhang, J.-G. Long Term Stability of Li-S Batteries Using High Concentration Lithium Nitrate Electrolytes. *Nano Energy* **2017**, *40*, 607–617.

(28) Zheng, T.; Zhu, B.; Xiong, J.; Xu, T.; Zhu, C.; Liao, C.; Yin, S.; Pan, G.; Liang, Y.; Shi, X.; Zhao, H.; Berger, R.; Cheng, Y.-J.; Xia, Y.; Müller-Buschbaum, P. When Audience Takes Stage: Pseudo-Localized-High-Concentration Electrolyte with Lithium Nitrate as the Only Salt Enables Lithium Metal Batteries with Excellent Temperature and Cathode Adaptability. *Energy Storage Mater.* **2023**, *59*, No. 102782.

(29) Liao, C.; Han, L.; Wang, W.; Li, W.; Mu, X.; Kan, Y.; Zhu, J.; Gui, Z.; He, X.; Song, L.; Hu, Y. Non-Flammable Electrolyte with Lithium Nitrate as the Only Lithium Salt for Boosting Ultra-Stable Cycling and Fire-Safety Lithium Metal Batteries. *Adv. Funct. Mater.* **2023**, *33* (17), No. 2212605.

(30) Jiang, Z.; Li, C.; Yang, T.; Deng, Y.; Zou, J.; Zhang, Q.; Li, Y. Fluorine-Free Lithium Metal Batteries with a Stable LiF-Free Solid Electrolyte Interphase. *ACS Energy Lett.* **2024**, *9* (4), 1389–1396.

(31) Xu, S.; Xu, S.; Guo, X.; Xiong, J.; Wei, Z.; Zhu, S.; Xu, J.; Gong, S.; Shi, P.; Guo, S.; Min, Y. Construction of a Fluoride-Free and High-Voltage Lithium Metal Battery with a Li3N/Li2O Heterostructure Solid Electrolyte Interface. *Adv. Funct. Mater.* **2025**, *35* (26), No. 2500335.

(32) Ramesh, S. L.; Lopez, J. Fluorine-Free Electrolytes for Lithium Metal Batteries: Challenges and Opportunities in Solvation Structure and Interphase Design. *ACS Energy Lett.* **2025**, *10* (4), 1671–1679.

(33) Guo, R.; Wang, D.; Zuin, L.; Gallant, B. M. Reactivity and Evolution of Ionic Phases in the Lithium Solid-Electrolyte Interphase. *ACS Energy Lett.* **2021**, *6* (3), 877–885.

(34) Ortiz Vitoriano, N.; Ruiz de Larramendi, I.; Sacci, R. L.; Lozano, I.; Bridges, C. A.; Arcelus, O.; Enterría, M.; Carrasco, J.; Rojo, T.; Veith, G. M. Goldilocks and the Three Glymes: How Na+ Solvation Controls Na–O2 Battery Cycling. *Energy Storage Mater.* **2020**, *29*, 235–245.

(35) Lecce, D. D.; Marangon, V.; Jung, H.-G.; Tominaga, Y.; Greenbaum, S.; Hassoun, J. Glyme-Based Electrolytes: Suitable Solutions for next-Generation Lithium Batteries. *Green Chem.* **2022**, *24* (3), 1021–1048.

(36) Xu, K.; Zhang, S. S.; Lee, U.; Allen, J. L.; Jow, T. R. LiBOB: Is It an Alternative Salt for Lithium Ion Chemistry? *J. Power Sources* **2005**, *146* (1), 79–85.

(37) Xu, K.; Zhang, S.; Poese, B. A.; Jow, T. R. Lithium Bis(Oxalato)Borate Stabilizes Graphite Anode in Propylene Carbonate. *Electrochem. Solid-State Lett.* **2002**, *5* (11), A259.

(38) Zhang, X.; Devine, T. M. Passivation of Aluminum in Lithium-Ion Battery Electrolytes with LiBOB. *J. Electrochem. Soc.* **2006**, *153* (9), B365.

(39) Xu, W.; Cooper, E. I.; Angell, C. A. Ionic Liquids: Ion Mobilities, Glass Temperatures, and Fragilities. *J. Phys. Chem. B* **2003**, *107* (25), 6170–6178.

(40) Ueno, K.; Yoshida, K.; Tsuchiya, M.; Tachikawa, N.; Dokko, K.; Watanabe, M. Glyme-Lithium Salt Equimolar Molten Mixtures: Concentrated Solutions or Solvate Ionic Liquids? *J. Phys. Chem. B* **2012**, *116* (36), 11323–11331.

(41) Shigenobu, K.; Shibata, M.; Dokko, K.; Watanabe, M.; Fujii, K.; Ueno, K. Anion Effects on Li Ion Transference Number and Dynamic Ion Correlations in Glyme–Li Salt Equimolar Mixtures. *Phys. Chem. Chem. Phys.* **2021**, *23* (4), 2622–2629.

(42) MacFarlane, D. R.; Forsyth, M.; Izgorodina, E. I.; Abbott, A. P.; Annat, G.; Fraser, K. On the Concept of Ionicity in Ionic Liquids. *Phys. Chem. Chem. Phys.* **2009**, *11* (25), 4962–4967.

(43) Hosaka, T.; Matsuyama, T.; Kubota, K.; Tatara, R.; Komaba, S. KFSA/Glyme Electrolytes for 4 V-Class K-Ion Batteries. *J. Mater. Chem. A* **2020**, *8* (45), 23766–23771.

(44) Brouillette, D.; Irish, D. E.; Taylor, N. J.; Perron, G.; Odziemkowski, M.; Desnoyers, J. E. Stable Solvates in Solution of Lithium Bis(Trifluoromethylsulfone)Imide in Glymes and Other Aprotic Solvents: Phase Diagrams, Crystallography and Raman Spectroscopy. *Phys. Chem. Chem. Phys.* **2002**, *4* (24), 6063–6071.

(45) Hobold, G. M.; Kim, K.-H.; Gallant, B. M. Beneficial vs. Inhibiting Passivation by the Native Lithium Solid Electrolyte Interphase Revealed by Electrochemical Li+ Exchange. *Energy Environ. Sci.* **2023**, *16* (5), 2247–2261.

(46) Wood, K. N.; Kazyak, E.; Chadwick, A. F.; Chen, K.-H.; Zhang, J.-G.; Thornton, K.; Dasgupta, N. P. Dendrites and Pits: Untangling the Complex Behavior of Lithium Metal Anodes through Operando Video Microscopy. *ACS Cent. Sci.* **2016**, *2* (11), 790–801.

(47) Menkin, S.; Fritzke, J. B.; Larner, R.; de Leeuw, C.; Choi, Y.; Gunnarsdóttir, A. B.; Grey, C. P. Insights into Soft Short Circuit-Based Degradation of Lithium Metal Batteries. *Faraday Discuss.* **2024**, *248*, 277–297.

(48) Adams, B. D.; Zheng, J.; Ren, X.; Xu, W.; Zhang, J.-G. Accurate Determination of Coulombic Efficiency for Lithium Metal Anodes and Lithium Metal Batteries. *Adv. Energy Mater.* **2018**, *8* (7), No. 1702097.

(49) Gunnarsdóttir, A. B.; Amanchukwu, C. V.; Menkin, S.; Grey, C. P. Noninvasive In Situ NMR Study of "Dead Lithium" Formation and

Lithium Corrosion in Full-Cell Lithium Metal Batteries. *J. Am. Chem. Soc.* **2020**, *142* (49), 20814−20827.

(50) Trease, N. M.; Zhou, L.; Chang, H. J.; Zhu, B. Y.; Grey, C. P. In Situ NMR of Lithium Ion Batteries: Bulk Susceptibility Effects and Practical Considerations. *Solid State Nucl. Magn. Reson.* **2012**, *42*, 62−70.

(51) Wang, Q.; Zhao, C.; Wang, S.; Wang, J.; Liu, M.; Ganapathy, S.; Bai, X.; Li, B.; Wagemaker, M. Clarifying the Relationship between the Lithium Deposition Coverage and Microstructure in Lithium Metal Batteries. *J. Am. Chem. Soc.* **2022**, *144* (48), 21961−21971.

(52) Aurbach, D.; Daroux, M. L.; Faguy, P. W.; Yeager, E. Identification of Surface Films Formed on Lithium in Dimethoxyethane and Tetrahydrofuran Solutions. *J. Electrochem. Soc.* **1988**, *135* (8), 1863.

(53) Menkin, S.; O'Keefe, C. A.; Gunnarsdóttir, A. B.; Dey, S.; Pesci, F. M.; Shen, Z.; Aguadero, A.; Grey, C. P. Toward an Understanding of SEI Formation and Lithium Plating on Copper in Anode-Free Batteries. *J. Phys. Chem. C* **2021**, *125* (30), 16719−16732.

(54) Melin, T.; Lundström, R.; Berg, E. J. Elucidating the Reduction Mechanism of Lithium Bis(Oxalato)Borate. *J. Phys. Chem. Lett.* **2024**, *15* (9), 2537−2541.

(55) Andersson, E. K. W.; Wu, L.-T.; Bertoli, L.; Weng, Y.-C.; Friesen, D.; Elbouazzaoui, K.; Bloch, S.; Ovsyannikov, R.; Giangrisostomi, E.; Brandell, D.; Mindemark, J.; Jiang, J.-C.; Hahlin, M. Initial SEI Formation in LiBOB-, LiDFOB- and LiBF4-Containing PEO Electrolytes. *J. Mater. Chem. A* **2024**, *12* (15), 9184−9199.

(56) Zhang, Q.; Wang, K.; Wang, X.; Zhong, Y.; Liu, M.; Liu, X.; Xu, K.; Fan, W.; Yu, L.; Li, W. Lithium Bis(Oxalate)Borate Reinforces the Interphase on Li-Metal Anodes. *ACS Appl. Mater. Interfaces* **2019**, *11*, 20854.

(57) Hernández, G.; Mogensen, R.; Younesi, R.; Mindemark, J. Fluorine-Free Electrolytes for Lithium and Sodium Batteries. *Batter. Supercaps* **2022**, *5* (6), No. e202100373.

(58) Xu, K.; Lee, U.; Zhang, S.; Wood, M.; Jow, T. R. Chemical Analysis of Graphite/Electrolyte Interface Formed in LiBOB-Based Electrolytes. *Electrochem. Solid-State Lett.* **2003**, *6* (7), A144.

(59) Maity, A.; Svirinovsky-Arbeli, A.; Buganim, Y.; Oppenheim, C.; Leskes, M. Tracking Dendrites and Solid Electrolyte Interphase Formation with Dynamic Nuclear Polarization—NMR Spectroscopy. *Nat. Commun.* **2024**, *15* (1), 9956.

(60) Michan, A. L.; Parimalam, B. S.; Leskes, M.; Kerber, R. N.; Yoon, T.; Grey, C. P.; Lucht, B. L. Fluoroethylene Carbonate and Vinylene Carbonate Reduction: Understanding Lithium-Ion Battery Electrolyte Additives and Solid Electrolyte Interphase Formation. *Chem. Mater.* **2016**, *28* (22), 8149−8159.

(61) Köcher, S. S.; Schleker, P. P. M.; Graf, M. F.; Eichel, R.-A.; Reuter, K.; Granwehr, J.; Scheurer, Ch. Chemical Shift Reference Scale for Li Solid State NMR Derived by First-Principles DFT Calculations. *J. Magn. Reson.* **2018**, *297*, 33−41.

(62) Cheng, D.; Wynn, T.; Lu, B.; Marple, M.; Han, B.; Shimizu, R.; Sreenarayanan, B.; Bickel, J.; Hosemann, P.; Yang, Y.; Nguyen, H.; Li, W.; Zhu, G.; Zhang, M.; Meng, Y. S. A Free-Standing Lithium Phosphorus Oxynitride Thin Film Electrolyte Promotes Uniformly Dense Lithium Metal Deposition with No External Pressure. *Nat. Nanotechnol.* **2023**, *18* (12), 1448−1455.